Journal of Space Safety Engineering 13 (2026) 349–362

Contents lists available at ScienceDirect

Journal of Space Safety Engineering

journal homepage: www.elsevier.com/locate/jsse

A coupled SPH–FEM strategy for hypervelocity impact analysis with emphasis on shock-wave transmission in Whipple shields

Tiziana Cardone [a,b,*], Chiara Bisagni [b,c]

[a] ESA/ESTEC, Keplerlaan 1, 2201 AZ Noordwijk, the Netherlands
[b] TU Delft, Faculty of Aerospace Engineering, Kluyverweg 1, 2629 HS Delft, the Netherlands
[c] Politecnico di Milano, Department of Aerospace Science and Technology, Via La Masa 34, 20156 Milano, Italy

ARTICLE INFO

Article history:
Received 13 November 2025
Received in revised form 25 February 2026
Accepted 23 March 2026
Available online 2 April 2026

Keywords:
Space debris
Hyper velocity impact
Whipple shield
Spacecraft integrity
Secondary debris cloud

ABSTRACT

The population of orbital debris in Low Earth Orbit (LEO) continues to increase steadily. This situation is driven by a combination of human space activities and collisions between objects in orbit, which are becoming increasingly unavoidable and pose a significant threat to space missions.

This work addresses debris–spacecraft collision phenomena by first investigating the hypervelocity impact of a projectile on a single plate. A coupled smoothed particle hydrodynamics (SPH) and finite element method (FEM) numerical framework, implemented in the commercial code LS-DYNA®, is developed to simulate this process and correlated with publicly available hypervelocity impact experimental data. The methodology is subsequently optimised and extended to a more complex configuration, namely a Whipple shield, which is more representative of realistic spacecraft shielding concepts against debris impacts. Validation is performed using an experimental dataset provided by Airbus Defence and Space.

Unlike conventional SPH/FEM coupling approaches that are primarily used to improve local damage modelling near the impact zone, the proposed framework is deliberately formulated to enable consistent propagation of shock waves and stress fields into the surrounding finite element domain. This enables the method to be employed not only for accurate fragmentation modelling, but as a physics-driven approach for analysing energy transport and shock propagation within spacecraft structures following hypervelocity impacts.

The developed methodology enhances insight into spacecraft structural behaviour under hypervelocity debris impacts and supports its application in the design and optimisation of future spacecraft shielding solutions.

1. Introduction

Throughout their operational lifetime, spacecraft can be subjected to collisions with meteoroids and human-made debris, particularly in Low Earth Orbit (LEO) [1]. According to ESA's MASTER-8 space debris environment model [2], average relative impact velocities in Low Earth Orbit are of the order of 10 km/s, while higher velocities may occur depending on orbital inclination and encounter geometry. Such impacts represent a significant threat to space missions, as debris and meteoroids carry sufficient kinetic energy to penetrate structural elements and damage spacecraft subsystems or payloads, potentially leading to mission failure.

Hypervelocity impact (HVI) phenomena are governed by parameters including projectile and target material properties, impact velocity, impact angle, and the mass, shape, and composition of the debris. Collisions are generally considered catastrophic when the energy-to-target-mass ratio (EMR) exceeds 40 J/g [3]. In such cases, the shock wave generated by the impact may propagate through the spacecraft structure with sufficient intensity to induce widespread fragmentation.

Assessing the effects of HVI is therefore essential to determine whether a spacecraft can withstand an impact and maintain mission operability.

Abbreviations: ADS, Airbus Defence and Space; BLE, Ballistic Limit Equation; EMR, Energy-to-target-Mass Ratio; EoS, Equation of State; ESA, European Space Agency; FEM, Finite Element Model; HVI, Hyper Velocity Impact; LEO, Low Earth Orbit; NASA, National Aeronautics and Space Administration; SPH, Smoothed-Particle Hydrodynamics.

* Corresponding author.
E-mail address: tiziana.cardone@esa.int (T. Cardone).

https://doi.org/10.1016/j.jsse.2026.03.005

1.1. Background and existing approaches

Interest in hypervelocity impact phenomena intensified during the development of the International Space Station and the Space Shuttle [4–6]. Early studies focused primarily on penetration assessment, aiming to determine whether debris would perforate structural panels. Extensive experimental campaigns led to the development of ballistic limit equations (BLEs) [7–9], which provide simplified relationships for estimating critical plate thicknesses required to prevent penetration. These equations have been incorporated into engineering tools such as PIRAT [10] and ESABASE2 [11], enabling rapid probabilistic assessments of penetration risk.

Complementary experimental investigations, such as those conducted by Piekutowski [12–14], provided detailed insight into impact physics through radiographic imaging of tests performed with two-stage light gas guns. These experiments documented projectile and bumper fragmentation, debris cloud formation, and secondary fragment evolution.

Empirical models have been derived from laboratory impact experiments and from observations of in-orbit fragmentation events. A prominent example is the NASA Standard Breakup Model, implemented in the EVOLVE 4.0 framework [15], which provides statistical descriptions of fragment generation in catastrophic collisions. The NASA Standard Breakup Model, originally implemented in the EVOLVE 4.0 framework [15], represents a major advancement in the statistical description of fragmentation processes resulting from on-orbit collisions and explosions. The model provides physically-based algorithms for predicting fragment size, mass, area-to-mass ratio distributions, and velocity dispersion following catastrophic breakups. Such modelling efforts have significantly improved long-term debris environment prediction capabilities and are widely used in population evolution tools for risk assessment and mitigation studies.

Semi-empirical models do not explicitly solve the full set of governing equations for hypervelocity impacts. Instead, they apply conservation principles of mass, momentum, and energy to reconcile a broad range of experimental results and ensure consistency [16,17]. Such approaches provide simplified and computationally efficient tools, requiring only limited input data. They are particularly advantageous when details of the colliding bodies or the event kinematics are scarce, and multiple scenarios must be investigated through repeated simulations. While computationally efficient, such methods provide limited insight into local stress fields or shock-wave propagation within the structure.

1.2. Numerical modelling of hypervelocity impacts

Numerical modelling approaches described in the literature generally fall into two categories: discrete element methods [18] and continuum-based techniques, such as the finite element method (FEM), Eulerian formulations [19,20], and smooth particle hydrodynamics (SPH) [21–23].

SPH is a mesh-free, Lagrangian method for the modelling of fluid flows and solid bodies and has already been used for the modelling of hypervelocity impacts of space debris [21]. Thomson [21] employed the SPH module in AUTODYN® to investigate projectile impact on multiple aluminium plates. In the simulations, this projectile is impacting several plates placed in parallel with the aim of finding the number of plates needed in order not to have a crater in the last plate [21]. The work of Sibeaud et al. [22] provides a collection of hyper velocity impact tests on a single plate. The tests were performed using a 2-stage light gas gun and consist of a single aluminium plate, fully clamped at the outer circumference, which is impacted by an aluminium sphere. The impact occurs at an angle perpendicular to the plate and at a velocity of 5.941 Km/s. Legaud et al. subsequently used these experiments to verify their numerical methodology [23]. In related work, Pai et al. [24] simulated hypervelocity impacts of 4-mm-diameter spherical projectiles on monolithic and coated plates using the AUTODYN® module of ANSYS®, considering impact speeds of 3.5 and 5.5 km/s.

While purely Lagrangian FEM approaches can simulate impact events, they may suffer from severe mesh distortion and non-physical fragmentation patterns under extreme deformation. To overcome these limitations, coupled SPH–FEM approaches have become widely adopted in computational impact mechanics.

1.3. Coupled SPH–FEM approaches and interface considerations

Coupled SPH–FEM methods combine the strengths of both formulations: SPH particles are used to describe highly localized regions near the impact zone, where large deformation and fragmentation dominate, while FEM is used to represent the surrounding structure and capture the global structural response with reduced computational cost.

This hybrid strategy enables accurate modelling of severe material distortion without excessive element erosion, which may otherwise lead to numerical instability or artificial fragment shapes in purely Lagrangian FEM simulations. Furthermore, SPH–FEM coupling allows the use of consistent constitutive models across both particle and element domains, preserving material behaviour continuity.

The compatibility between SPH and FEM formulations has been discussed extensively in the literature. He et al. [25] showed that the principal differences between the two approaches lie primarily in the evaluation of strains, strain rates, and internal forces, facilitating their integration within unified computational frameworks. More recent studies, such as Heberling et al. [19] and Ceri et al. [26], have applied interface-based SPH–FEM coupling in hydrocode simulations of hypervelocity impact experiments, demonstrating the suitability of such approaches for capturing impact-induced deformation and stress-wave propagation.

Despite these advantages, coupled SPH–FEM methods are not without limitations. The interface between particle and element domains represents a critical region where displacement continuity, stress transfer, and numerical stability must be carefully enforced. Poor interface treatment may lead to artificial stress concentrations, numerical noise, or spurious wave reflections. Addressing these issues is essential, particularly when the objective extends beyond local fragmentation analysis to include reliable stress-wave transmission into the surrounding structure.

1.4. Objective and contribution of the present work

This paper presents a numerical methodology, based on a coupled SPH/FEM approach, to understand what happens to a spacecraft orbiting in LEO when it is hit by a hypervelocity space debris. Numerically, the impact event is modelled as a spherical projectile striking a double-plate configuration, commonly referred to as a Whipple shield [23], representative of typical spacecraft panel arrangements.

The adopted strategy relies on an interface-based SPH–FEM coupling, in which the impact region is discretised using SPH particles to capture severe deformation and fragmentation, while the surrounding structure is modelled using finite elements to enable extraction of global structural response and stress-wave propagation

The proposed modelling technique is dedicated to understanding the transfer of energy from the impacted area to the rest of the Whipple shield (and therefore to the spacecraft).

The proposed modelling technique is first demonstrated with a replication of the work of Sibeaud et al. [22] and Legaud et al.

[23] on hypervelocity impacts of a sphere on a single plate and is validated against these literature experiments and simulations. The numerical methodology is then implemented to investigate a Whipple shield configuration and is validated thanks to a new set of data, courtesy of Airbus Defence and Space (ADS).

The proposed methodology analyses the impact considering both the dynamics and the thermo-mechanical loads. The parts involved in the impact are modelled taking into account their material and the thermal properties. The impact is modelled as a local event with the aim of reproducing the large deformation that occurs during an impact.

The ultimate objective is to establish a robust and repeatable modelling framework capable of predicting not only local damage but also the stress and energy transmitted to adjacent structural components, thereby supporting the design of debris-resilient spacecraft architectures.

It is emphasised that the present study does not aim at deriving generalised ballistic limit trends or statistically representative scaling laws across a broad hypervelocity impact parameter space. Instead, a deliberately controlled impact configuration is selected in order to isolate and investigate the behaviour of the coupled SPH–FEM interface and the associated mechanisms of debris cloud formation, energy transfer, and stress-wave propagation.

2. Problem description

A hypervelocity space-debris impact on a spacecraft first involves the external structural panel, which in shielding terminology is referred to as the bumper. Upon impact, the impacting debris perforates and fragments the bumper, generating a secondary debris cloud. This debris cloud propagates downstream and may strike internal spacecraft components, potentially causing further damage.

The spacecraft configuration considered in the present study is illustrated in Fig. 1. The outer spacecraft panel is treated as the bumper. Behind it, the internal equipment cover panel (e.g. enclosing avionics units such as batteries, Power Conditioning and Distribution Unit or other bus subsystems) is modelled as the rear wall. To evaluate the residual hazard after interaction with the rear wall, a third structural element is considered, acting as a witness plate. In the analysed configuration, this corresponds to the central structural tube. This component is of particular importance, as it typically accommodates the propellant tank. Perforation of the central tube may therefore allow secondary fragments to impact the pressurised tank, potentially leading to catastrophic failure.

To reproduce this impact scenario in a controlled laboratory environment, an equivalent Whipple-shield configuration is employed. This setup consists of parallel plates clamped at their perimeter, impacted by a spherical projectile launched using a two-stage light-gas gun [27]. The laboratory configuration replicates the functional roles of the spacecraft elements described above, enabling controlled investigation of debris-cloud formation, rear-wall interaction, and fragment transmission toward the witness plate.

3. Hybrid SPH–FEM methodology and coupling strategy

To capture the hypervelocity interaction between debris and a Whipple shield, a hybrid numerical approach combining the finite element method (FEM) and Smoothed Particle Hydrodynamics (SPH) is employed.

Smoothed Particle Hydrodynamics is a mesh-free, particle-based Lagrangian method particularly suited for modelling problems involving large deformations and fragmentation [28]. In the SPH formulation, the continuum is discretised into a set of particles that carry the state variables of the system (e.g. mass, velocity, stress, internal energy). A kernel approximation is used to evaluate spatial derivatives, allowing field variables and their gradients to be computed from weighted interactions between neighbouring particles through a smoothing function.

Each particle interacts with nearby particles within a defined influence domain. By weighting these interactions, continuous field quantities can be reconstructed at the particle location from the values of the surrounding particles. This characteristic makes SPH especially suitable for simulating hypervelocity impacts, where extreme deformation and material failure occur.

In the present methodology, SPH is used to model both the impacting projectile and the directly affected region of the target. The surrounding structural domain is discretised using FEM. This hybrid SPH/FEM coupling enables accurate representation of local fragmentation and material erosion while allowing the stress waves and energy transmitted beyond the impact zone to be consistently propagated through the adjacent structure.

The numerical model has been developed using the commercial code LS-DYNA®.

The coupling between the SPH and FEM regions is implemented through an interface contact algorithm, which enforces kinematic compatibility along the shared boundary:

$$\Gamma_{Interface} = \Omega_{FEM} \cap \Omega_{SPH} \tag{1}$$

A dedicated hybrid interface zone is defined in this region, in which SPH particles are constrained to move consistently with adjacent finite elements. This ensures continuity of displacement and velocity fields across the interface and enables reliable transmission of stresses and momentum from the SPH domain into the FEM structure.

Within the hybrid interface zone, SPH particles "*i*" interact with both neighbouring particles and finite elements within their support domain, defined by the smoothing length "*h*". This configuration smooths the transition between the two formulations and reduces common interface-related issues reported in the literature, such as artificial stress concentrations, numerical noise, or spurious wave reflections.

4. Numerical modelling of hypervelocity impact on a single plate

The numerical methodology has been developed first considering the impact of a projectile on a single plate (the bumper). To establish the methodology, the authors have reproduced the experimental test data performed by Sibeaud et al. [22] using a two-stage light gas gun in operation at the Centre d'Etudes de Gramat (CEG) and already numerically simulated by Legaud et al. [23]. These tests provide well-documented experimental measurements and constitute a suitable validation benchmark for the SPH–FEM coupling strategy. The objective of this replication is to establish physical consistency of the coupling strategy under controlled and well-documented conditions.

4.1. Experimental configuration reproduced

One representative test case from the Sibeaud campaign was selected. In this configuration, a spherical projectile with 10 [mm] diameter impacts a single plate (bumper) with dimensions 150×150×2 [mm], both in Al6061-T6, at a velocity of 5.941 km/s under normal incidence. The experimental setup is schematically reproduced in Fig. 3, and the principal physical parameters are summarised in Table 1.

4.2. Experimental validation metrics

In the experimental campaign, the following debris cloud characteristics were measured at $t = 16$ µs after impact:

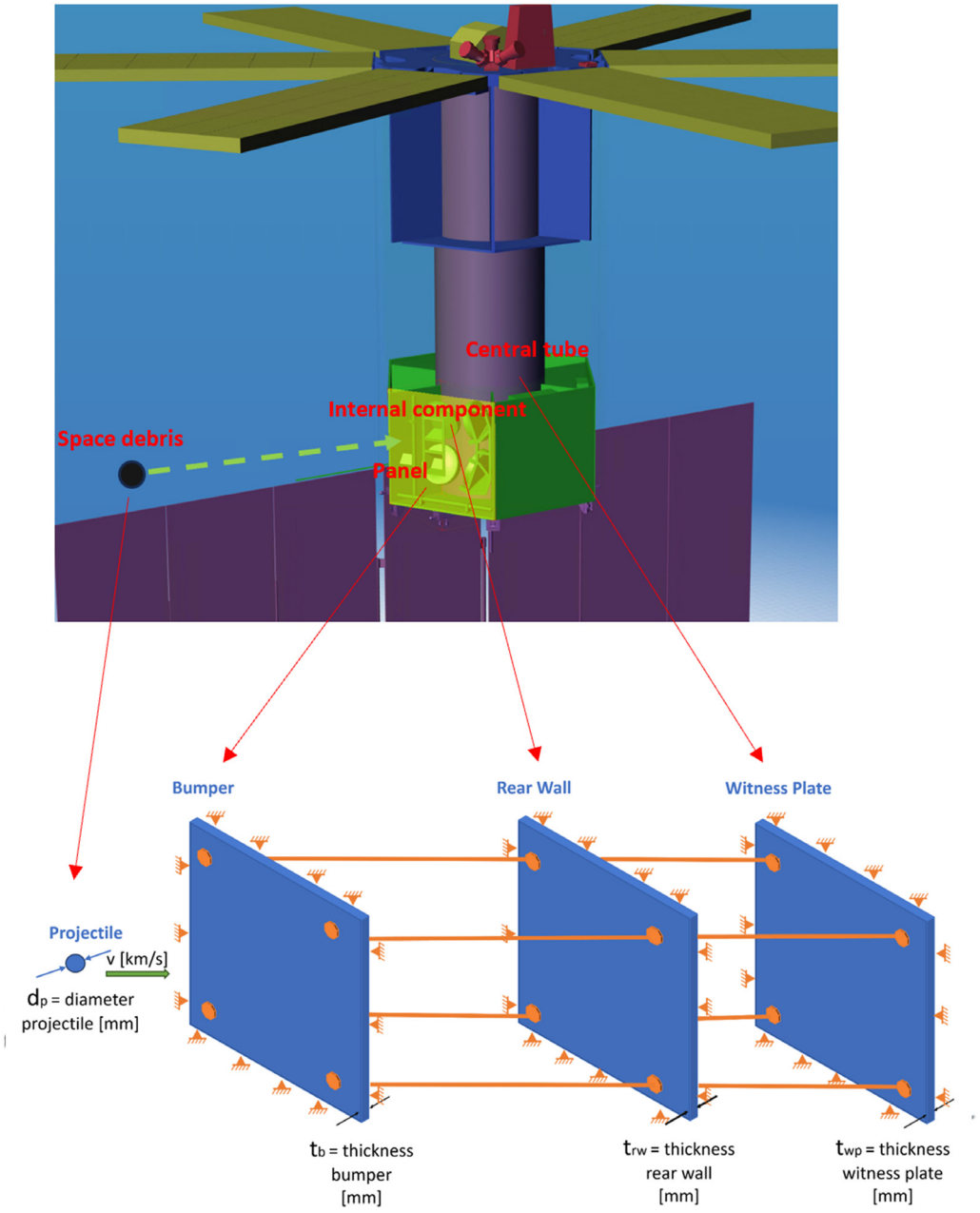

Fig. 1. Whipple Shield Configuration (Courtesy of ESA).

Table 1
Sibeaud's test set-up physical characteristics.

Physical parameters	Value
Projectile Diameter	10 mm
Projectile Velocity	5.941 km/s
Impact angle	0° (normal impact)
Dimensions of the impacted plate	150×150×2 mm

Table 2
Sibeaud HVI experimental test results at 16 µs.

Parameter	Symbol	Value
Debris cloud length	LDC	81.1 mm
Debris cloud front velocity	VDC,front	4.8 km/s
Debris cloud maximum diameter	DDC,max	65.6 mm
Crater diameter in bumper	Dcr	18.9 mm

- Debris cloud length, L_{DC}
- Debris cloud front velocity, $V_{DC,front}$
- Maximum debris cloud diameter, $D_{DC,max}$
- Crater diameter in the target plate, D_{cr}

These geometric descriptors are illustrated in Fig. 4 and are reported in Table 2.

These quantities constitute the primary validation metrics for the SPH domain before extending the methodology to the Whipple shield configuration.

The purpose of this validation exercise is not to reproduce an extensive ballistic database, but to verify the physical consistency of the SPH domain and its coupling behaviour under well-

characterised and traceable experimental conditions. By comparing debris cloud geometric descriptors (length, maximum diameter, front velocity, and crater diameter) with experimental measurements, the modelling framework is assessed in terms of its ability to reproduce fragmentation dynamics and momentum transfer mechanisms prior to analysing stress-wave propagation within the FEM domain. The validation performed is therefore mechanistic in nature, rather than statistical validation of ballistic limit performance.

4.3. Numerical model and discretisation strategy

To reduce computational cost while preserving physical fidelity, only one quarter of the experimental configuration was modelled, following the approach of Legaud et al. [23]. Symmetry boundary conditions were applied along the two orthogonal planes (Fig. 5).

The modelled plate dimensions were 75 × 75 × 2 mm. The central 25 × 25 mm impact region was discretised using SPH particles to capture severe deformation and fragmentation. The surrounding region was modelled using Lagrangian solid finite elements.

The SPH discretisation consisted of:

- Bumper: 200 × 200 × 26 particles (640,000 total)
- Projectile: 80 × 40 × 40 particles (67,024 total)

The transition SPH/Lagrange is guaranteed by a tied contact between particles and finite elements. The connection between components is implemented by defining the contact slave set as the external SPH nodes bordering the finite elements model of the plate's external zone, and the master set as the segment set of finite elements faces within the plate model's external zone that share borders with the internal SPH plate domain. This configuration creates a tied linkage, restricting the elements and nodes translational degrees of freedom. In LS-DYNA®, tied contact conditions are readily available, constraining slave nodes to move in unison with the master surface. Initialization involves projecting each slave node orthogonally onto the nearest master segment. If the defined tolerance is satisfied, the nodes are adjusted to the master surface without introducing artificial stresses, thus compensating for minor geometric discrepancies.

During the simulation, each slave node maintains a fixed relative position with respect to its corresponding master segment. To correctly represent this phenomenon, it is important to model the behavior of the material during and after the impact, specifying the adopted fracture criteria [24–29] and the Equation of State [30].

4.4. Constitutive modelling and failure criteria

Legaud et al. employed the Steinberg material model in their simulations [30–32]. In contrast, this study adopts the Johnson–Cook model, to represent strain hardening, strain-rate sensitivity, and thermal softening under large deformation and high strain-rate conditions [32–34].

In this formulation, strain hardening, strain-rate dependence, and thermal softening are captured within a unified expression. Strain hardening refers to the increase in strength and hardness of ductile metals as they undergo plastic deformation. This process is associated with the creation and movement of dislocations—irregularities in the crystal lattice. As dislocations accumulate and hinder one another's motion, the material becomes progressively more resistant to deformation. The resulting strain-hardened state is characterised by a higher yield stress, but reduced ductility.

Strain-rate effects become important in high-speed events, as rapid deformation alters the stiffness of the material. This influence is particularly pronounced when the projectile velocity exceeds the material's speed of sound. Thermal softening, in turn, links the material properties to temperature. The Johnson–Cook model [30] combines these contributions in the following equation:

$$\sigma_y = \left(A + B\bar{\varepsilon}^{p^n}\right)\left(1 + c ln\varepsilon^*\right)\left(1 - T^{*m}\right) \tag{2}$$

with:

$$T^* = \frac{T - T_{room}}{T_{melt} - T_{room}} \tag{3}$$

where σ_y denotes the yield stress, $\bar{\varepsilon}^p$ the effective plastic strain, and A, B, n, c and m are material constants, T is the current temperature, $T_{room}$is the reference room temperature and T_{melt} is the melting temperature of the material. The first term,A, represents the initial yield stress. The second term $B\bar{\varepsilon}^{p^n}$, accounts for strain hardening, describing the increase in strength with plastic deformation. The third term introduces the effects of thermal softening and damage accumulation.

The original experiments employed Al 2017 as the projectile material and Al 6061-T6 for the impacted plate. For the simulations, however, both elements were represented with Al 6061-T6 data, since suitable constitutive parameters for Al 2017 were not available and the two alloys exhibit comparable properties.

Material splitting, cracking, and tensile failure are represented in the simulation through the spalling model implemented in LS-DYNA®. The material physically spalls when the maximum pressure is higher than or equal to the cut-off pressure:

$$\sigma_{\max} \geq -\sigma_{\mathrm{p}} \tag{4}$$

When spallation takes place, tensile stresses in the affected material are reset to zero, though compressive stresses can still be carried. The deviatoric components of stress are removed, ensuring that hydrostatic tension cannot arise. In this way, any calculated tensile pressures vanish, and the spalled material is treated as debris.

The values implemented in the simulations are reported in Tables 3 and Table 4.

Table 3
Material properties of Al 6061-T6 aluminum alloy.

Material Property	Symbol	Value
Density	P	2.703 g/cm^3
Elastic Modulus	E	69 GPa
Shear Modulus	G	27.6 GPa
Poisson's Ratio	N	0.33
Melting Temperature	T_m	792 K
Reference Temperature	T_0	273 K
Specific heat	c_p	875 J/kgK

Table 4
Johnson-Cook material model parameters for Al 6061-T6 aluminum alloy.

Johnson-Cook parameters	Symbol	Value
Yield Stress	A	324.1 MPa
Strain Hardening parameter	B	113.8 MPa
Strain Hardening exponent	N	0.42
Strain Rate parameter	C_{JC}	0.002
Thermal Softening exponent	M	1.34
Pressure Cut-off	σ_p	−1200 MPa
Spall type	SPALL	2.0

4.5. Equation of state

A hypervelocity impact is characterized by very high pressures and temperatures. To describe the state of the material under its physical conditions, the Mie-Gruneisen equation of state (EoS) has been chosen [35,36]. The EoS is the mathematical description of

Table 5
Mie-Gruneisen EoS parameters.

Mie-Gruneisen parameters	Value
C	5328 m/s
S1	1.4
S2	0
S3	0
Gruneisen parameter γ_0	1.97
a factor	0.48
Initial internal energy (10^{-5} J)	0
Initial relative volume	0

the material behaviour for a given set of initial conditions. The Grüneisen equation of state defines the pressure of a compressible material (P) by establishing a linear relation between shock velocity and particle velocity, expressed as:

$$P = \frac{\rho C^2 \mu \left[1 + \left(1 - \frac{\gamma_0}{2}\right)\mu - \frac{a}{2}\mu^2\right]}{1 - (S_1 - 1)\mu - S_2 \frac{\mu^2}{\mu+1} - S_3 \frac{\mu^3}{(\mu+1)^2}} + (\gamma_0 + a\mu)e \quad (5)$$

Where:

C is the Y-intercept of the vs-vp curve and represents bulk sound speed; (vs is the velocity of the shock wave; vp is the velocity of the particle)

S1, S2 and S3 are the coefficients of the vs-vp curve's slope;

γ_0 refers to Gruneisen coefficient; a is the first order correction to γ_0;

ρ is the material density;

$\mu = \frac{\rho}{\rho_0} - 1$.

The parameters describing the hypervelocity impact in the analysis are tabulated in Table 5.

It should be noted that the Mie–Grüneisen equation of state is known to present limitations at very high impact velocities (typically above ∼5 km/s for aluminium–aluminium impacts), particularly when strong phase changes, melting, or vaporisation effects become dominant. In such regimes, more advanced multiphase or tabulated equations of state may provide improved thermodynamic accuracy.

In the present study, the Mie–Grüneisen formulation was selected because the primary objective is not to resolve detailed phase transitions or vaporisation phenomena, but to ensure a stable and physically consistent representation of shock generation and stress-wave transmission into the surrounding structure. The focus of this work lies on energy transport and structural response within the coupled SPH–FEM framework, rather than on the exact thermodynamic state of the fragmented material.

The impact velocities investigated in this paper range from 2.9 km/s to 7.1 km/s. Within this range, the Mie–Grüneisen formulation remains widely adopted in engineering-oriented hypervelocity simulations and provides an adequate description of the pressure–volume response for the purpose of stress-wave propagation analysis. The limitations of the EoS at higher velocities are therefore acknowledged, but they do not compromise the main objectives of the present study.

4.6. SPH control and numerical stability

The control settings applied to the SPH particles play a central role in determining the stability, accuracy, and efficiency of the simulation by defining the particle interactions. In all the presented simulations, a *CONTROL_SPH card was used to manage SPH particle properties, including the activation of a particle deactivation box. This box effectively deactivates SPH particles that have gone outside the box and are no longer interacting with the structure, optimizing computational efficiency while capturing key impact features such as the evolving debris cloud and ejecta veil.

The SPH control algorithm dynamically adjusts the number of neighbors per particle during the computation, significantly exceeding the default value of 150. LS-DYNA's automatic adjustment of this value allowed the simulation to proceed to the final stages. If the number of neighbors per particle increases too much, the automatic process of neighbor determination leads to a program crash, so that it is necessary to update the initial default value.

Regarding the SPH formulation, Legaud et al. [23] concluded that the default SPH formulation is optimal for hyper-velocity impacts. The *CONTROL_SPH settings further define the interparticle interaction. The default "particle approximation" is used. According to this setting, particles of two different parts interact with the same mechanics as particles of the same part interact internally, ensuring accurate collision detection and debris cloud dynamics. Artificial viscosity played a key role in addressing discontinuities and preventing tensile instability. The choice of the Monaghan formulation over the standard solid-element artificial viscosity formulation proved to be more widely applicable due to the complex nature of the impact zones, as the solid-structure approximation fell short. Finally, incremental stabilization was implemented as total stabilization is only recommended for hyperelastic materials.

In addition, *SECTION_SPH card settings were used to control the SPH smoothing function and the smoothing length constant "h" (ref. Fig. 2). The use of an initial value of 1.2, bounded between 0.2 and 1.5 during the simulation, allowed for effective control of the particle dynamics. The cubic spline function was implemented as the kernel function of choice.

The plate area surrounding the impact zone requires the use of finite elements to limit computational effort. For proper finite element functionality, modeling cards different from those associated with SPH must be implemented. In this context, *SECTION_SOLID is used to satisfy the finite element attributes. Despite the thin composition of the bumper plate, shell elements were not considered due to the potential complications arising from their interaction with SPH. The main aspect that requires attention in the section card is the choice of the element formulation.

The constant stress solid element was chosen because of its accuracy, efficiency, and adaptability to large deformations. However, its use requires hourglass stabilization, which is implemented through the *CONTROL_HOURGLASS tab. The use of the Flanagan-Belytschko viscous form type [37] within this stabilization method proves to be suitable for very high-speed scenarios. This specific viscosity type is recommended in the LS-DYNA manual and has been defined in the literature [38] as optimal for hyper-velocity simulations. A major advantage is its negligible effect on the system energy, which increases its suitability for such simulations.

The termination time of the simulation is controlled by the mandatory *CONTROL_TERMINATION card in LS-DYNA, which allows tunability based on the simulation objectives. For the single wall scenario, a simulation duration of 20 µs is sufficient to capture the entire event, given the initial high projectile velocity defined by the *INITIAL_VELOCITY_GENERATION card. No further termination criteria were specified.

5. Validation of the numerical modelling technique against the simulations results from Legaud

Validation of the numerical approach was achieved through comparison between simulation outcomes and the experimental results reported by Sibeaud at $t = 16$ µs after impact. The percentage of the error of the authors' simulations towards Sibeaud's experiments is reported in Table 6, showing a very good match between simulations and experiments.

For completeness, the qualitative view of the secondary debris cloud obtained in the simulation is presented in Fig. 6, where a lateral view (perpendicular to the impact velocity direction) is shown.

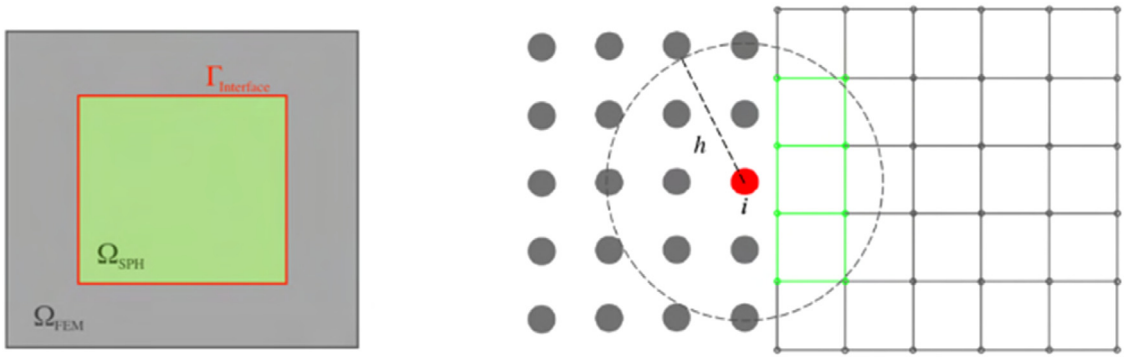

Fig. 2. FEM-SPH interface contact coupling domain discretization example: (left) domain discretization, (right).

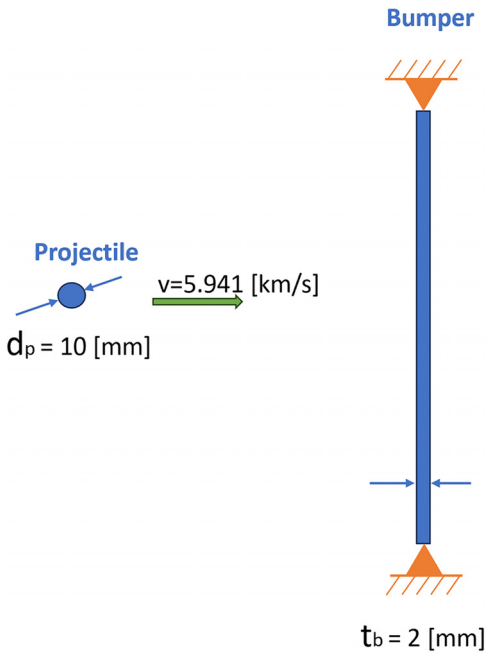

Fig. 3. Representation of Sibeaud's experiment setup.

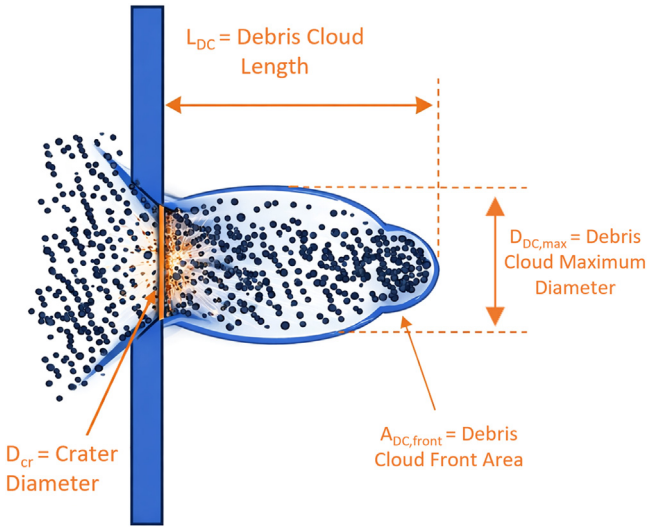

Fig. 4. Sibeaud experiment parameters.

The figure illustrates the early formation of the debris cloud within the first microseconds after impact. Already at 1 µs, an outer radially expanding envelope of fine fragments can be observed. This expanding outer layer, commonly referred to as the ejecta veil, corresponds to the high-angle component of the debris cloud generated by shock-driven fragmentation of the projectile and bumper material. At 2 µs, the debris cloud becomes established. By 4,6 and 8 µs a pronounced mass concentration is visible at the core and leading edge of the cloud, primarily composed of projectile material (yellow), surrounded by a more dispersed layer of fragmented plate material (green). The continued expansion of the ejecta veil

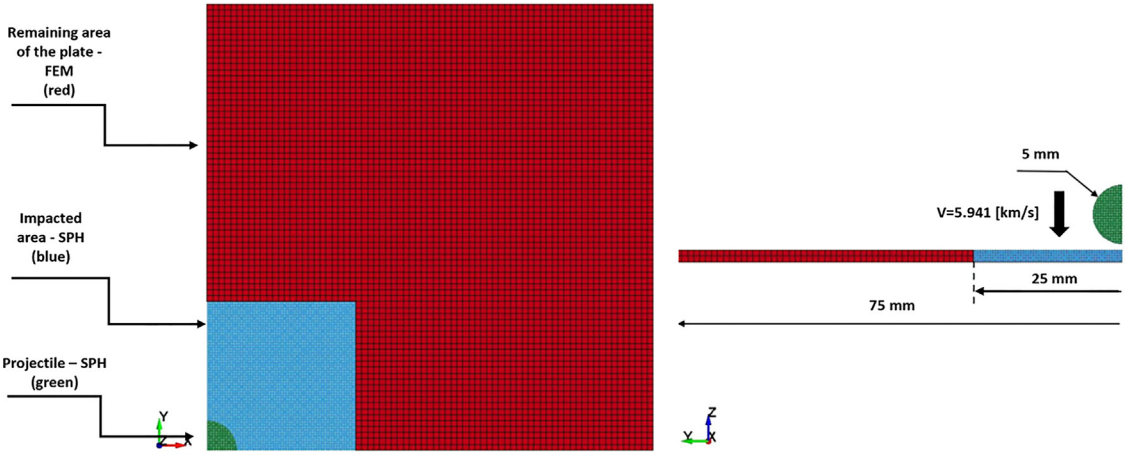

Fig. 5. details of the mesh used in the simulation of the experiments of Sibeaud et al.

Table 6
Sibeaud tests results vs. Authors numerical results.

HVI parameters	Symbol	%error between Sibeaud experimental results and authors simulation results
debris cloud length	L_{DC}	0.1%
debris velocity at the cloud front	$V_{DC,front}$	0.7%
cloud maximum diameter	$D_{DC,max}$	5.8%
crater diameter in the plate	D_{cr}	0.5%

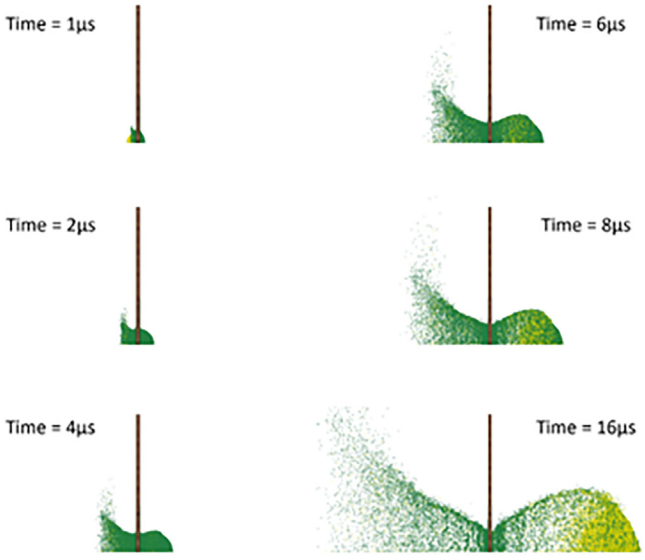

Fig. 6. HVI on single plate. Evolution of debris cloud in the first 16μs.

at 16 μs illustrates the progressive spatial redistribution of mass in the impact direction.

6. Numerical model of a Whipple shield configuration

The numerical modelling technique has been further developed by the authors with the aim of numerically representing the hypervelocity impact test scenario of a space debris impact on a spacecraft, initially described in Fig. 1 and known as the Whipple shield configuration.

To properly represent this scenario, the authors have chosen to model the bumper plate and the rear wall as full plates (no quarter models) to simplify the boundary conditions. The witness plate is not simulated, as it is present in the experiments mainly for practical reasons, to collect any debris generated and to avoid damaging the test facility and instrumentation.

To support the model setup and the subsequent validation of the modelling technique, the input data and results of a test campaign carried out by ADS at the Ernst Mach Institute have been used. These data are provided by courtesy of ADS.

The experiments set-up is reported in Fig. 7 and consists of two plates of Al2024-T3 placed at 60 mm distance and an aluminium projectile of 5 mm diameter. The experiments are run a different projectile impact velocities and the authors have reproduced only the ones at impact velocity 2.9 km/s (test a), 5.9 km/s (test b) and 7.1 km/s (test c).

These three cases were selected because they span distinct physical regimes of hypervelocity impact behaviour. The 2.9 km/s case represents a lower-velocity penetration regime with limited fragmentation, the 5.9 km/s case corresponds to a fully fragmenting but energetically moderate regime, and the 7.1 km/s case represents a higher-energy condition characterised by extensive projectile breakup and increased rear-wall damage.

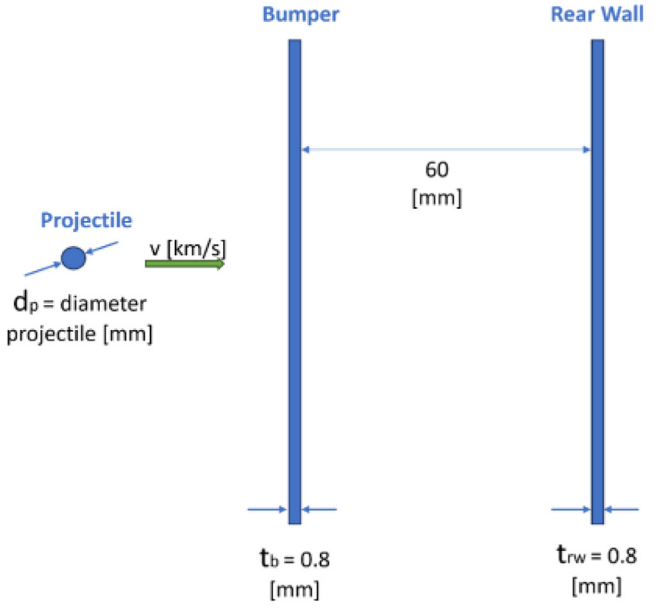

Fig. 7. experimental data set configuration (credits Airbus Defence and Space GmbH).

By selecting these three impact velocities, the model is assessed across a transition from partial to complete fragmentation, enabling evaluation of the robustness of the SPH–FEM coupling under progressively increasing shock intensity and energy transfer.

The mesh characteristics of the model have been summarised in Table 7, taking into account the following aspects:

- The projectile, a 5-mm diameter sphere, has been modelled entirely with SPH particles, since it undergoes near-complete disintegration upon impact with the bumper.
- The accuracy of debris cloud prediction has been ensured by applying a high-density mesh in the bumper impact region.
- The bumper has been represented as a 30 × 30 mm plate instead of the full 100 × 100 mm geometry, as the event is highly localised. This has allowed dense meshing through the thickness and in-plane directions without excessive computational cost. From the single-plate simulations, it has been verified that crater edges remain sufficiently distant from model boundaries, ensuring no influence on debris cloud formation.
- Because the debris cloud originates from a relatively small bumper volume interacting with the projectile, through-thickness discretisation has been prioritised. In the current model, the SPH zone has been defined with 26 particles through the thickness, while the FE zone has been meshed with four elements, resulting in an aspect ratio of two.
- Insights from the single-plate HVI simulations have shown that the secondary debris cloud is significantly larger than the original projectile and propagates about 15% slower. To capture this effect, the rear wall has been modelled larger than the bumper, with the SPH zone centred in the same way as for the bumper (Fig. 8).
- To model the HVI on a Whipple shield, the authors propose to define a hybrid (or transition) zone between SPH particles and FEM elements to smooth the transition and allow more accurate stress propagation to the finite elements. The SPH particles and finite elements are active from the start of the impact. The hybrid elements are SPH particles that are not

Table 7
Whipple shield model - mesh details.

Elements	Dimensions of SPH zone (mm)	Number of SPH particles in impact direction	Total number of SPH particles in the part
Projectile	$D = 5$	40×40×40	33,552
Bumper	30×30×0.8	250×250×12	691,200
Rear wall	100×100×0.8	350×350×10	1225,000

Table 8
Comparison test data vs. simulation results.

Test	Projectile diameter (mm)	Impact Velocity (km/s)	Bumper hole diameter (mm)			Rear wall hole diameter (mm)		
			test	**Simulation**	**%error**	**test**	**simulation**	**%error**
Test-a	5.0	2.9	6.7	7.5	0.11%	27.0	25.0	0.07%
Test-b	5.0	5.4	8.1	8.5	0.05%	24.0	33.0	0.37%
Test-c	5.0	7.1	9.3	9.1	0.02%	58.0	52.0	0.1%

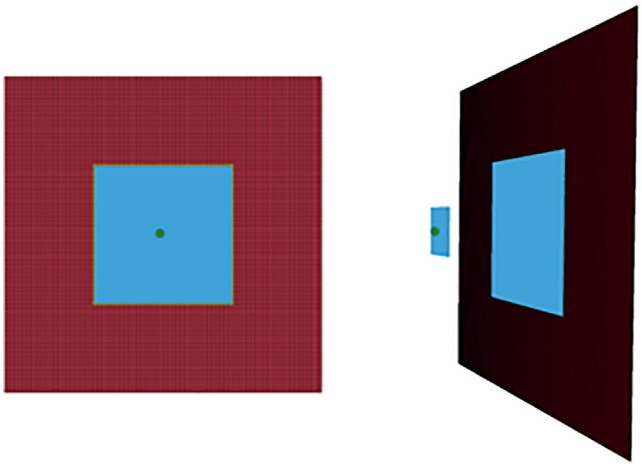

Fig. 8. Projectile (green), bumper (blue), rear wall solid FE zone (red) and SPH zone (blue): (left) front view; (right) isometric view.

active for coupling until the moment of failure of the finite element. In this way, the mass and momentum of the failed elements are retained because they don't disappear but are replaced by one or more SPH particles. The hybrid zone of the bumper is shown in yellow in Fig. 9.

The Johnson-Cook model is adopted. Both bumpers are made of Al 2024-T3, whereas the projectile is made from Al 2007. For the last aluminium, Johnson-Cook parameters are not easily available, therefore in the simulation it is considered that also the projectile is made of Al 2024-T3. This approximation in the simulation is based on the consideration that both Al 2024-T3 and Al 2007 are high-strength, heat-treatable alloys but have differences. Al 2024-T3 is an aluminium-copper-iron alloy with a yield strength of around 275 MPa and has its density and properties in general are comparable to Al 2007. Al 2024-T3 has slightly higher yield strength but this has minimal effects on the results, as the yield strength is not the driving parameter in the penetration.

The same EoS as in the simulation of the impact on one plate has been used.

7. Validation of the numerical model of the Whipple shield configuration against the test data

The simulation results for the three tested velocities have been reported in Table 8 and compared with the empirical data. It is emphasised that the selected test cases are representative configurations chosen to evaluate the predictive capability of the coupled SPH–FEM framework under controlled conditions. The objective is not to demonstrate agreement across a statistically broad database of Whipple shield experiments, but to verify that the modelling approach consistently reproduces key physical mechanisms governing debris fragmentation, cloud evolution, and penetration behaviour. This focused validation strategy ensures traceability between experimental conditions and numerical setup while maintaining clarity regarding the configuration-specific scope of the conclusions.

In particular, the diameters of the holes, both in the bumper and in the rear wall, are compared and show a good agreement between experiment and simulation.

The results for all three velocities of the ADS data set are shown in Fig. 10, viewed from the rear of the rear wall, to better highlight the crater dimensions and hole shapes obtained in the simulations. The bumper holes have been observed to remain nearly circular. A qualitative inspection of the damage morphology reveals that the rear wall exhibits irregular openings and cracks, with large fractures that prevent the definition of a single representative perforation diameter.

The results have further indicated that, for aluminium projectiles impacting aluminium plates, velocities above 4 km/s lead to complete projectile fragmentation, melting, and crater material ejection.

For these three velocity cases, the evolution of the velocity of the secondary debris cloud within the first 16 µs is obtained via the simulation and represented in Fig. 11, with the view in the direction transversal to the impacted plate.

The debris expelled beyond the bumper has been found to consist mainly of plate material (red) rather than projectile material (green). The properties of the central projectile zone (green) govern the destructive potential of the debris cloud. At all three studied velocities, most of the projectile material is directed towards the cloud front. Higher velocities generate a larger number of secondary fragments due to the increased impact energy. While the ejected particles pose a long-term orbital debris hazard, they also help dissipate energy and reduce the likelihood of projectile penetration into the spacecraft unit (rear wall in the experiments).

As it can be seen in Fig. 10, together with the secondary debris cloud, formed in the direction of the impact, also a primary debris bubble is formed in the opposite direction of the impact, behind the bumper. This primary debris cloud consists of a combination of projectile (green particles) and bumper material (red particles). It can be noticed that the projectile material is at the centre of the debris cloud, surrounded by the plate material, both in the impact direction as well as at the opposite direction.

The results of these simulations have been further exploited by extracting the values of the velocity of the particles of the secondary debris cloud and the stress generated on the FEM elements of the first panel. This information is not available from the test

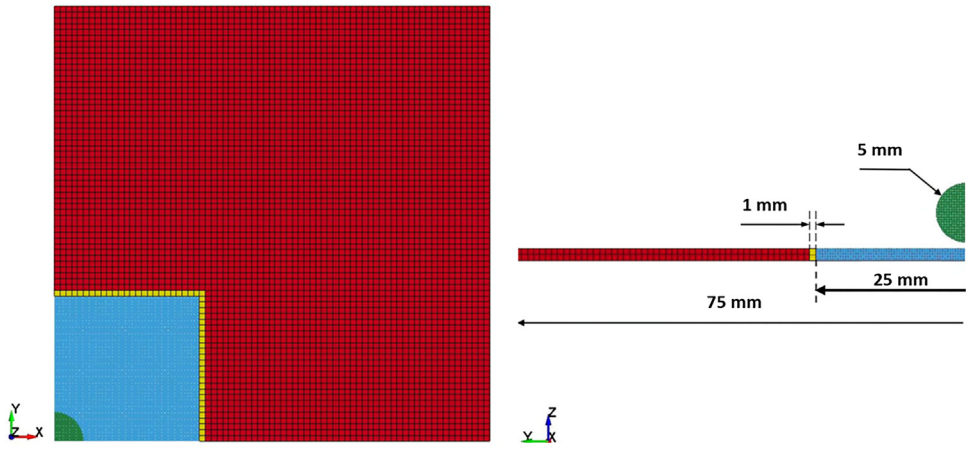

Fig. 9. modelling of the hybrid zone, represented in yellow, data set from ADS GmbH.

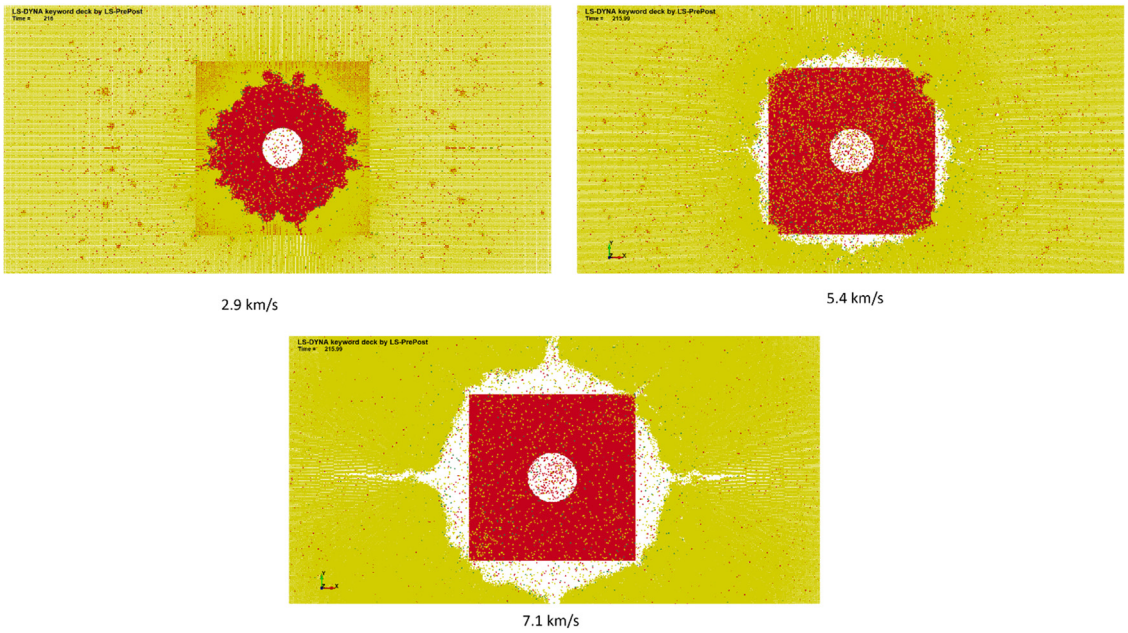

Fig. 10. view from the rear of the crater of rear wall (yellow) and the bumper (red) a) at impact velocity 2.9 km/s, b) at impact velocity 5.4 km/s, c) at impact velocity 7.1 km/s.

data set provided and cannot be compared with real data. The velocity of the secondary debris cloud allows an understanding of the energy of the secondary debris cloud hitting the rear panel (representing the unit inside the spacecraft). The stress levels of the FEM element of the bumper provide information on the stresses transmitted to the spacecraft. These physical parameters make it possible to understand how and if the debris impact has affected the structural integrity of spacecraft elements close to the impact zone (e.g. mechanical joints, mechanisms, optical payloads, etc.…).

The leading edge of the debris cloud is formed by the fastest particle. The destructive potential depends on the correlation between fragment velocity and mass distribution: a cloud with significant mass at peak velocity is more damaging than one dominated by slower fragments.

Behind the bumper, the velocity profile shows that most of the cloud mass travels at more than 80% of the impact speed. This distribution can be quantified by counting particles in the high- and low-velocity zones. Since each particle retains constant density and volume, the particle count directly reflects the mass at a given velocity.

Fig. 12 shows the velocity profile at the three different impact velocities in a view transverse to the impacted plates. It can be seen that the particles at the front of the cloud have a higher velocity than those trailing behind. This quantitative method provides an insight into the mass distribution that determines the destructive power of the debris cloud.

For an impact velocity of 2.9 km/s, over 80% of the primary debris cloud is composed of elements with velocities greater than 90% of the impact velocity. This means that most of the mass in the cloud has retained the high velocity of the impact. The secondary debris cloud shows a different behaviour: less than 2% of its mass retains velocities above 90% of the initial impact speed. If not contained by the rear wall, the cloud continues to propagate through the cavity at reduced velocity. At 8 µs, the leading edge travels faster than after its interaction with the rear wall at 16 µs.

The rear wall captures the debris over a wider area, significantly reducing cloud velocity, demonstrating the high effectiveness of the Whipple shield in absorbing impacts.

Fig. 12 compares the evolution of the secondary debris cloud for different initial impact velocities (2.9 km/s, 5.4 km/s and 7.1 km/s),

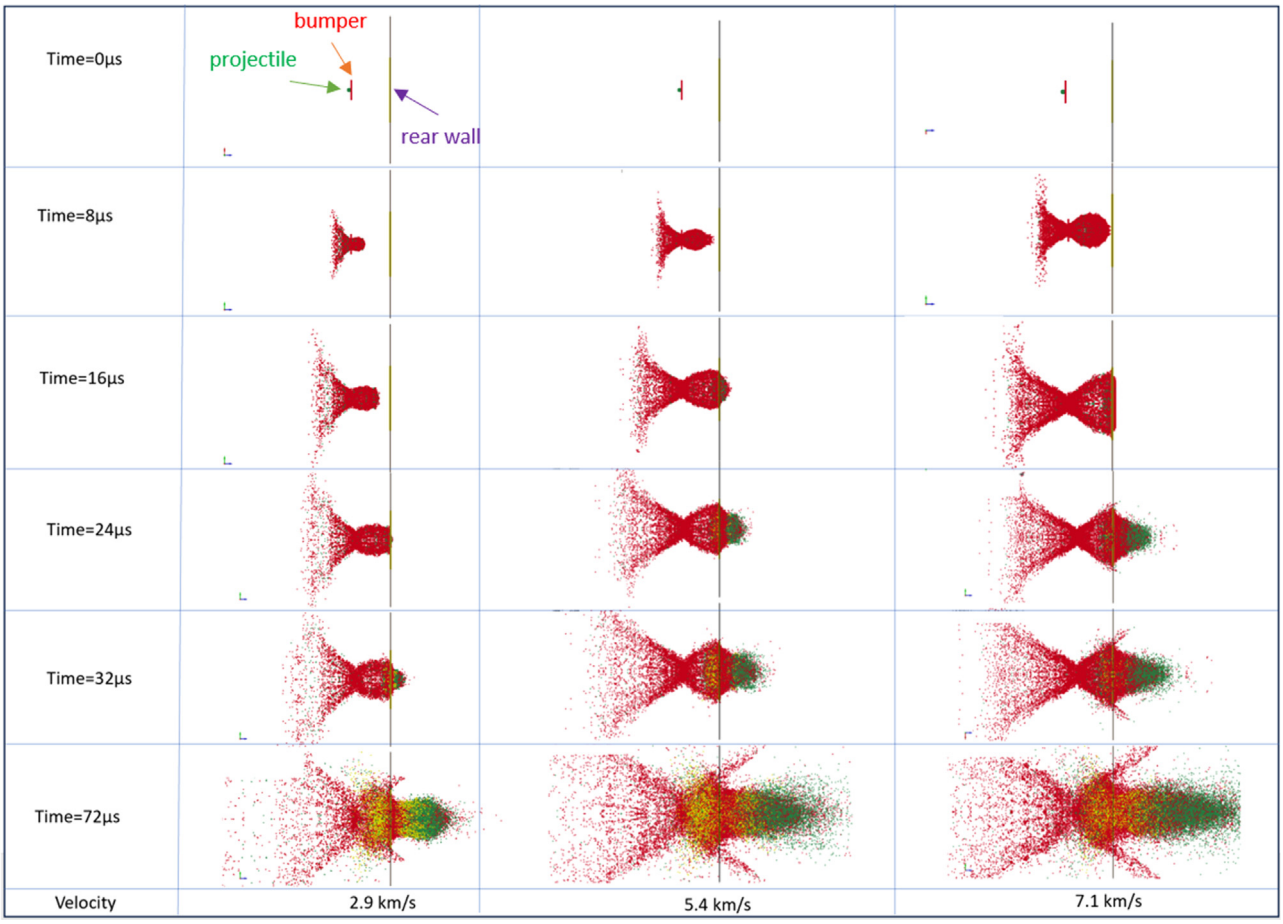

Fig. 11. Time evolution of the secondary debris cloud for three initial impact velocities (2.9 km/s, 5.4 km/s and 7.1 km/s). Snapshots are reported at different times after impact (0–72 µs). Distances are shown in the impact plane and time is expressed in microseconds (µs).

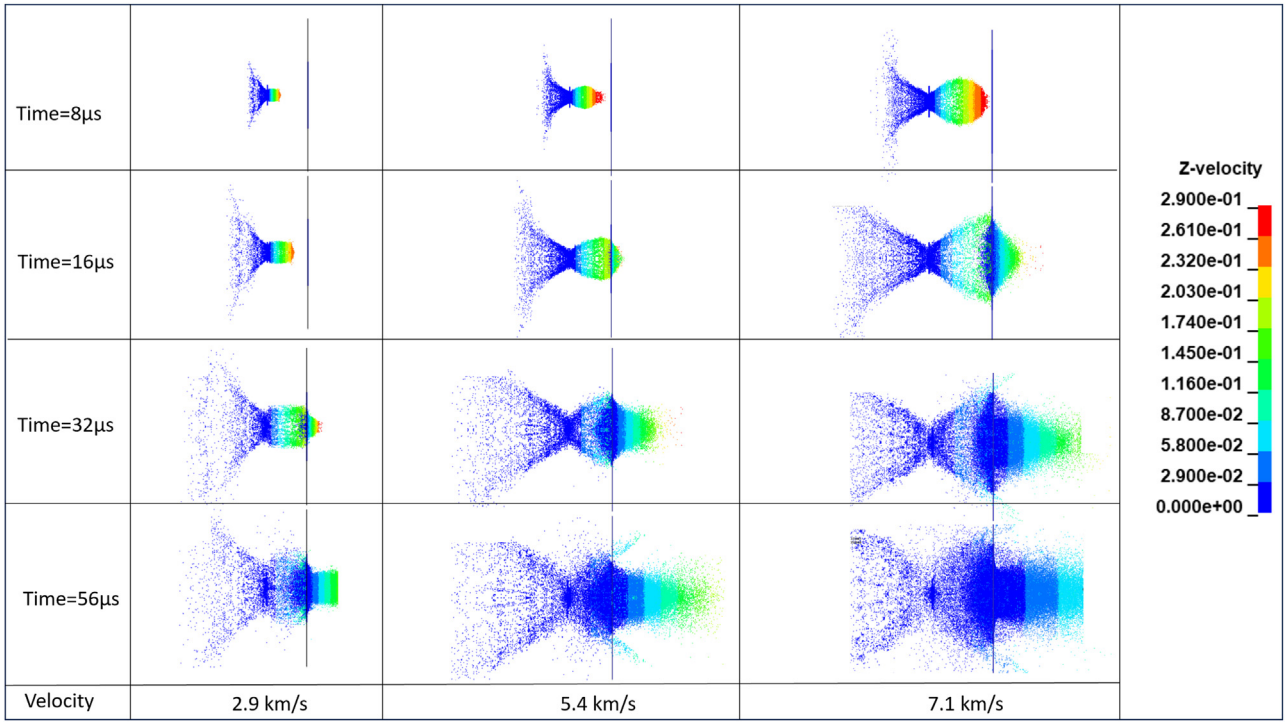

Fig. 12. Time evolution of the secondary debris cloud for three initial impact velocities (2.9 km/s, 5.4 km/s and 7.1 km/s). The colour scale represents the Z-component of fragment velocity expressed in km/s. Time is reported in microseconds (µs).

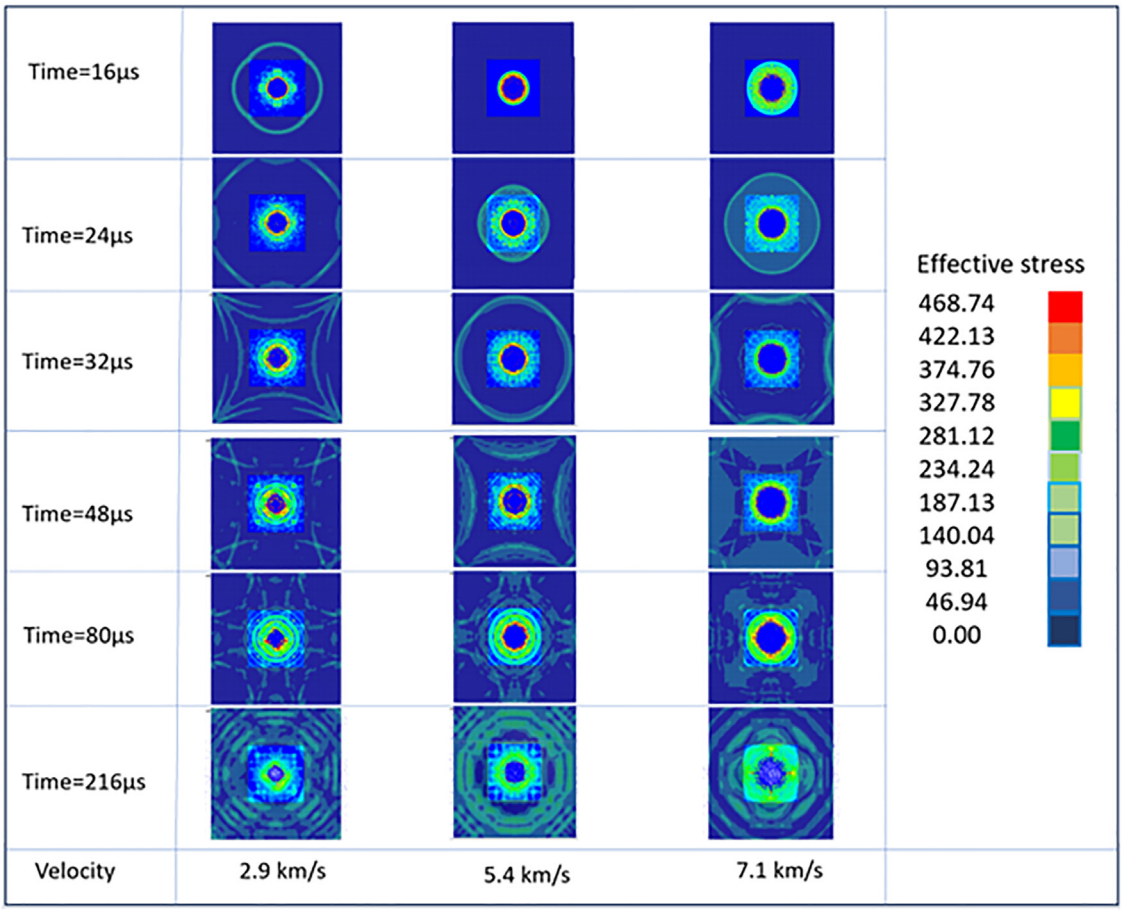

Fig. 13. Von Mises stress field evolution fringe plots for 3 different impact velocities.

with the color scale representing the Z-component of fragment velocity in km/s. This velocity component, aligned with the impact direction, is used as an indicator of the damage potential of the debris cloud.

It can be seen that at 7.1 km/s, the cloud formed after the impact on the rear wall is much larger than the clouds formed for initial velocities of 2.9 km/s and 5.4 km/s. Most of the mass of the secondary cloud moves at less than 20% of the initial velocity. This behaviour changes at higher velocities, because at higher impact velocities the energy involved in the impact is also higher. This is an important finding because the energy involved in the impact determines the damage potential of the secondary cloud.

The Von Mises stress fringe plots of the rear wall are reported in Fig. 13 for the three velocities analysed at different time steps. The stresses on the rear wall are plotted (measured in MPa). Despite the absence of direct experimental stress measurements, the numerical results have offered useful insight into the stress field.

Once the rear wall is impacted by the secondary debris cloud, the stress spreads from the centre of the plate in a circular manner, until the border of the plate. The interaction between waves can be observed by studying the stress, leading to peaks and valleys of stress within the structure. The limits of the fringe plot are set such that the red zones are near the yield strength of the material.

These results also show that the projectile velocity exceeds the speed of sound within the bumper material. The shockwave propagating through the material is reflected at the target surfaces and reverses direction. The overlap of incident and reflected waves can locally raise stresses beyond material strength, leading to cracking or spall separation at high velocities.

8. Conclusions

This paper addressed the problem of hypervelocity space debris impact on spacecraft structures. A coupled SPH/FEM modelling technique was proposed to numerically represent this highly complex phenomenon, in which both the projectile and the impacted structure undergo severe fragmentation, large deformations, and possible material state changes.

Within the proposed framework, the fragmentation process and the associated physical and kinematic evolution of debris fragments are modelled using SPH, while the energy transfer to the structure and the resulting stress propagation in the remaining parts of the panel are captured using FEM. This hybrid approach allows the detailed modelling of the impact zone while preserving the capability to analyse the structural response at a larger scale.

A key advantage of the methodology is its practical applicability at spacecraft level. Only local modifications of an existing spacecraft FEM model are required: the region of interest around the impact is discretised with SPH, whereas the rest of the model can remain unchanged. This makes the approach compatible with standard industrial modelling practices.

The methodology was first established and calibrated using numerical simulations and test data available in the literature for single-plate impact configurations. It was subsequently extended to a more complex and representative Whipple shield configuration and further correlated with a new set of hypervelocity impact tests performed on Whipple shield specimens and kindly provided by Airbus Defence and Space GmbH.

The proposed modelling methodology implies that an appropriate material model and equation of state are implemented in the

modelling, including an appropriate fracture criterion. In the simulation, the Johnson–Cook material model and the Mie–Grüneisen equation of state were implemented. While the latter presents known limitations at extreme hypervelocity regimes involving significant phase transitions, it proved adequate for the engineering-oriented objectives of this study, focused on shock-wave transmission and structural response.

Particular attention was given to the SPH–FEM transition region to ensure correct energy transfer between the two domains, as improper coupling may lead to loss of physically relevant information.

After comparing the simulations with the selected test configurations, the proposed numerical methodology was found to be accurate within the investigated parameter space. The results should be interpreted as a configuration-specific demonstration of the modelling framework, rather than as a generalised parametric study of Whipple shield performance.

Beyond perforation assessment, the simulations were used to derive the velocity profile of the secondary debris cloud and to evaluate the stress field at the rear wall. Direct experimental correlation of the computed stress histories was not possible, as energy-related measurements were not available in the provided test dataset.

To address this limitation, a dedicated test campaign is planned, including instrumentation of the test specimen with shock sensors and digital image correlation systems. This will enable measurement of shock propagation within the structure and reconstruction of the stress field in the bumper during impact.

In a further step, the methodology will be extended to a spacecraft-like structural configuration. A dedicated experimental campaign will be designed to simultaneously characterise the generated debris cloud (mass, velocity, fragment size distribution) and the internal shock-wave propagation.

The combined numerical and experimental effort will allow closing the validation loop and will provide clearer indications on how the proposed SPH/FEM framework can be applied in support of spacecraft design and verification activities in operational programmes.

Declaration of competing interest

The authors declare that they have no known competing financial interests or personal relationships that could have appeared to influence the work reported in this paper.

CRediT authorship contribution statement

Tiziana Cardone: Writing – review & editing, Writing – original draft, Visualization, Validation, Supervision, Resources, Project administration, Methodology, Investigation, Formal analysis, Data curation, Conceptualization. **Chiara Bisagni:** Writing – review & editing, Supervision.

Acknowledgments

The authors gratefully acknowledge Airbus Defence and Space GmbH for providing the data used to validate the simulations.

The authors gratefully thank Mateusz Harazim, for his valuable contribution to the numerical simulation during his master thesis at TU Delft.

References

[1] ESA Space Debris Office“ESA’s Annual Space Environment Report”, European Space Agency, Darmstadt, Germany, 2023 Tech. Rep. https://www.sdo.esoc.esa.int/environment_report/Space_Environment_Report_latest.pdf accessed 30 August 2025.

[2] S. Flegel, et al., MASTER-8: The ESA Meteoroid and Space Debris Terrestrial Environment Reference Model, ESA Space Debris Office, ESOC, Darmstadt, Germany, 2018.

[3] A. Francesconi, C. Giacomuzzo, L. Olivieri, G. Sarego, A. Valmorbida, D. McKnight, “Examination of satellite collision scenarios spanning low to hypervelocity encounters using semi-empirical models”, IAC-19-A6.3.8, 2019.

[4] M.E. Kalinski, “Hypervelocity impact analysis of International Space Station Whipple and enhanced stuffed Whipple shields”, 2004, 12. https://hdl.handle.net/10945/1233 (accessed 30 August 2025).

[5] E.L. Christiansen, Investigation of hypervelocity impact damage to space station truss tubes, Int. J. Impact Eng. 10 (1990) 125–133, doi:10.1016/0734-743X(90)90053-X.

[6] E.L. Christiansen, J.L. Hyde, R.P. Bernhard, Space Shuttle debris and meteoroid impacts, Adv. Space Res. 34 (2004) 1097–1103, doi:10.1016/j.asr.2003.12.008.

[7] W.P. Schonberg, Concise history of ballistic limit equations for multi-wall spacecraft shielding, Reach 1 (2016) 46–54, doi:10.1016/j.reach.2016.06.001.

[8] E.L. Christiansen, J.H. Kerr, Ballistic limit equations for spacecraft shielding, Int. J. Impact Eng. 26 (2001) 93–104, doi:10.1016/S0734-743X(01)00070-7.

[9] National Research CouncilProtecting the Space Station from Meteoroids and Orbital Debris, The National Academies Press, Washington, DC, 1997, doi:10.17226/5532.

[10] S. Kempf, F.K. Schäfer, T. Cardone, I. Ferreira, S. Gerené, R. Destefanis, L. Grassi, Simplified spacecraft vulnerability assessments at component level in early design phase at the European Space Agency's Concurrent Design Facility, Acta Astronaut 129 (2016) 291–298, doi:10.1016/j.actaastro.2016.08.014.

[11] ESABase2, 2025. accessed 30 August accessed 30 August https://esabase2.net .

[12] A.J. Piekutowski, A simple dynamic model for the formation of debris clouds, Int. J. Impact Eng. 10 (1990) 453–471, doi:10.1016/0734-743X(90)90079-B.

[13] A.J. Piekutowski, Characteristics of debris clouds produced by hypervelocity impact of aluminum spheres with thin aluminum plates, Int. J. Impact Eng. 14 (1993) 573–586, doi:10.1016/0734-743X(93)90053-A.

[14] A.J. Piekutowski, Formation and description of debris clouds produced by hypervelocity impact, NASA Contractor Report 4707 (1996) https://hadlandimaging.com/wp-content/uploads/2021/06/NASA-CR4707-Report-1996.pdf. accessed 30 August 2025.

[15] N.L. Johnson, P.H. Krisko, J.-C. Liou, P.D. Anz-Meador, NASA's new breakup model of EVOLVE 4.0, Adv. Space Res. 28 (2001) 1377–1384, doi:10.1016/S0273-1177(01)00423-9.

[16] D. McKnight, R. Maher, L. Nagl, Refined algorithms for structural breakup due to hypervelocity impact, Int. J. Impact Eng. 17 (1995) 547–558, doi:10.1016/0734-743X(95)99879-V.

[17] A. Francesconi, C. Giacomuzzo, L. Olivieri, G. Sarego, M. Duzzi, F. Feltrin, A. Valmorbida, K.D. Bunte, M. Deshmukh, E. Farahvashi, J. Pervez, M. Zaake, T. Cardone, D. de Wilde, CST: a new semi-empirical tool for simulating spacecraft collisions in orbit, Acta Astronaut 160 (2019) 195–205, doi:10.1016/j.actaastro.2019.04.035.

[18] E. Watson, J.-L. Sandoval Murillo, M. Büttner, P. Matura, M. Schimmerohn, Simulating hypervelocity impact with a discrete element approach, Acta Astronaut 199 (2022) 425–435, doi:10.1016/j.actaastro.2022.07.044.

[19] T. Heberling, G. Terrones, W. Weseloh, Hydrocode simulations of a hypervelocity impact experiment over a range of velocities, Int. J. Impact Eng. 122 (2018) 1–9, doi:10.1016/j.ijimpeng.2018.07.019.

[20] W.P. Schonberg, Aluminum 2219-T87 and 5456-H116: a comparative study of spacecraft wall materials in dual-wall structures under hypervelocity impact, Acta Astronaut 26 (1992) 799–812, doi:10.1016/0094-5765(92)90061-M.

[21] D. Thomson, Conceptual Design of a Space Vehicle for Orbital Debris Protection, University of Manitoba, 2013 Master's thesis http://hdl.handle.net/2099.1/24505 accessed 30 August 2025.

[22] J.-M. Sibeaud, P.L. Héreil, V. Albouys, Hypervelocity impact on spaced target structures: experimental and ouranos simulation achievements, Int. J. Impact Eng. 29 (2003) 647–658, doi:10.1016/j.ijimpeng.2003.10.012.

[23] T. Legaud, M.Le Garrec, N. Van Dorsselaer, V. Lapoujade, “Improvement of satellites shielding under high velocity impact using advanced SPH method”, in: 12th European LS-DYNA® Users Conference, 2019. https://api.semanticscholar.org/CorpusID:236173235 (accessed 30 August 2025).

[24] A. Pai, A. Sharma, I.M. Eby, C.R. Kini, S.B. Shenoy, A numerical approach for response of Whipple shields with coated and monolithic front bumper to hypervelocity impact by spherical projectiles, Acta Astronaut 202 (2023) 433–441, doi:10.1016/j.actaastro.2022.10.041.

[25] Q. He, X. Chen, J. Chen, Finite element–smoothed particle hydrodynamics adaptive method in simulating debris cloud, Acta Astronaut 175 (2020) 99–117, doi:10.1016/j.actaastro.2020.05.056.

[26] S. Ceri, Z.S. Khodaei, Numerical investigation of hypervelocity impact simulation with FEM/SPH formulation for space structures, Int. J. Impact Eng. 187 (2024) 104926, doi:10.1016/j.ijimpeng.2024.104926.

[27] B. Lexow, M. Wickert, K. Thoma, F. Schäfer, M.H. Poelchau, T. Kenkmann, The extra-large light-gas gun of the Fraunhofer EMI: applications for impact cratering research, Meteorit. Planet. Sci (2013) accessed 30 August 2025, doi:10.1111/j.1945-5100.2012.01427.x.

[28] J.L. Lacome, Ch. Espinosa, Simulation of hypervelocity spacecrafts and orbital debris collisions using smoothed particle hydrodynamics in LS-DYNA®, 2001. (conference) accessed 30 August 2025 https://www.dynalook.com/conferences/european-conf-2001/simulations-of-hypervelocity-impacts-with-smoothed.pdf .

[29] X.-T. Zhang, X.-G. Li, T. Liu, G.-H. Jia, Element fracture technique for hypervelocity impact simulation, Adv. Space Res. 55 (2015) 2293–2304, doi:10.1016/j.asr.2015.01.040.
[30] D.J. Steinberg, Equation of State and strength properties of selected materials, (publication), 1996. https://worldcat.org/title/54089938 (accessed 30 August 2025).
[31] D.J. Steinberg, S.G. Cochran, M.W. Guinan, A constitutive model for metals applicable at high-strain rate, J. Appl. Phys. 51 (1980) Issue 3accessed 30 August 2025, doi:10.1063/1.327799.
[32] J. Peng, C. Hu, Y. Li, L. Zhang, F. Jing, Determination of parameters of Steinberg-Guinan constitutive model with shock wave experiments, Int. J. Mod. Phys. B 22 (2008) 1111–1116, doi:10.1142/S0217979208046396.
[33] G.R. Johnson, W.H. Cook, "A constitutive model and data for metals subjected to large strains, high strain rates and high temperatures", in: Proc. 7th Int. Symp. on Ballistics, The Hague, The Netherlands, April 1983, pp. 541–547.
[34] V.K.R. Sirigiri, V.Y. Gudiga, U.S. Gattu, G. Suneesh, K.M. Buddaraju, A review on Johnson Cook material model, Mater. Today: Proc. 62 (2022) 3450–3456, doi:10.1016/j.matpr.2022.04.279.
[35] O. Heuzé, General form of the Mie–Grüneisen equation of state, C. R. Méc. 340 (2012) 679–687, doi:10.1016/j.crme.2012.10.044.
[36] Livermore Software Technology Corporation (LSTC), LS-DYNA® Keyword User's Manual, Version 971, Vol. I, Livermore, CA, USA, 2007.
[37] T. Rabczuk, T. Belytschko, S.P. Xiao, Stable particle methods based on lagrangian kernels, Comput. Methods Appl. Mech. Eng. 193 (2004) 1035–1063.
[38] P. Plassard, J. Mespoulet, P.L. Héreil, Hypervelocity impact of aluminium sphere against aluminium plate: experiment and LS-DYNA correlation, in: Proc. 8th European LS-DYNA Users Conf., Strasbourg, France, 2011.